

Effects of roughness on the strength and fracturing processes in Mortar-Granite interface under tensile loading



GeoCalgary
2022 October
2-5
Reflection on Resources

Ghasem Shams¹, Patrice Rivard¹, Omid Moradian^{2,3}

¹ *Civil Engineering Department– Université de Sherbrooke, Sherbrooke, Québec, Canada*

² *Department of Earth Sciences, Swiss Federal Institute of Technology (ETH), Zurich, Switzerland*

³ *Civil Engineering Department, Colorado School of Mines, Golden, Colorado, USA*

ABSTRACT

Tensile failure and detachment of rock-concrete interfaces in civil engineering structures, such as gravity dams, are considered critical factors in controlling the stability of these structures. Despite many studies on the effect of the interface's roughness on the shear strength of such bi-material structures, very few studies have investigated the influence of the roughness on the rock-concrete interfaces under tensile loading. In this study, acoustic emission (AE) and digital image correlation (DIC) techniques were used to evaluate the effect of the interface's roughness on the strength and the fracture properties of granite-mortar specimens under direct tensile loading. Our results showed that the tensile strength of the rock-mortar interfaces increases with the interface's roughness. AE data revealed that the generated macroscopic fracture is composed of only tensile microcracks for specimens with a smooth interface, while it is composed of both tensile and shear microcracks for rough interface specimens. Since microcracks are more resistant to shear than tensile failure, the increase in the number of shear microcracks with interface roughness explains the increase in tensile strength with roughness. Specimens with rough interfaces also showed more ductile fracturing behavior. The DIC results indicated that the fracture process zone is mainly concentrated along the interface, while the final fractures did not pass those strain concentration zones. In contrast, the AE process zone better determined the location of the macroscopic fractures. Our results suggest that the AE measurements can explain why we get different strength values for the same material in similar experiments (e.g., rock-mortar specimens with rough and smooth interfaces). The findings of this study can improve our understanding of the tensile strength and behavior of rock-concrete interfaces, leading to the safer design of engineering structures.

RÉSUMÉ

La rupture en traction et le détachement des interfaces roche-béton dans les ouvrages de génie civil, tels que les barrages poids, sont considérés comme des facteurs critiques dans le contrôle de la stabilité de ces ouvrages. Malgré de nombreuses études sur l'effet de la rugosité de l'interface sur la résistance au cisaillement de telles structures bi-matériaux, très peu d'études ont étudié l'influence de la rugosité sur les interfaces roche-béton sous chargement de traction. Dans cette étude, des techniques d'émission acoustique (AE) et de corrélation d'images numériques (DIC) ont été utilisées pour évaluer l'effet de la rugosité de l'interface sur la résistance et les propriétés de rupture des échantillons de granit-mortier sous une charge de traction directe. Nos résultats ont montré que la résistance à la traction des interfaces roche-mortier augmente avec la rugosité de l'interface. Les données AE ont révélé que la fracture macroscopique générée est composée uniquement de microfissures de traction pour les spécimens à interface lisse, alors qu'elle est composée à la fois de microfissures de traction et de cisaillement pour les spécimens à interface rugueuse. Les microfissures étant plus résistantes au cisaillement qu'à la rupture en traction, l'augmentation du nombre de microfissures de cisaillement avec la rugosité de l'interface explique l'augmentation de la résistance à la traction avec la rugosité. Les échantillons avec des interfaces rugueuses ont également montré un comportement de fracturation plus ductile. Les résultats du DIC ont indiqué que la zone de processus de fracture est principalement concentrée le long de l'interface, tandis que les fractures finales ne traversaient pas ces zones de concentration de déformation. En revanche, la zone de processus AE a mieux déterminé la localisation des fractures macroscopiques. Nos résultats suggèrent que les mesures AE peuvent expliquer pourquoi nous obtenons différentes valeurs de résistance pour le même matériau dans des expériences similaires (par exemple, des spécimens de roche-mortier avec des interfaces rugueuses et lisses). Les résultats de cette étude peuvent améliorer notre compréhension de la résistance à la traction et du comportement des interfaces roche-béton, conduisant à une conception plus sûre des structures d'ingénierie.

1 INTRODUCTION

In many geomechanics projects, where concrete structures are built on or in rocks, such as concrete gravity dams, the rock-concrete (RC) interface appears as the potential zone of crack initiation and ultimate failure. The RC structures that are often subjected to combined tension, compression, and shear stress states could fail along the interfacial zone putting the entire project at risk. Therefore, many studies have been performed to evaluate the mechanical properties of the RC interface in recent decades.

The literature review indicates that the mechanical properties of the RC interface have been primarily studied under compression [1], [2], and shear [3]–[8] loading. However, despite the critical importance of tensile strength (TS) in governing the failure of engineering materials, including RC structures [9]–[11], very few studies have dealt with the tensile interaction mechanism of the rock-concrete interfaces. A reliable understanding of the RC behaviour under tension is essential to provide a safe design of elements incorporating RC interfaces. For example, the tensile strength of the dam-foundation interface controls the overturning moment at the toe zone of the dam [12], [13]. Furthermore, the tensile failure at the rock-shotcrete interface is often the primary failure mode in underground excavations [14]–[17].

To date, two principal test methods, among others, have been applied to determine the tensile strength of brittle materials such as rock and concrete. These include the direct tension test (DT) [2], [18]–[20] and the Brazilian test (BT) [1], [15], [21].

The direct tensile strength (DTS) of bi-material specimens has been evaluated by several researchers for core samples of rock-concrete interfaces with different diameters and different rock types [2], [5], [16], [22]. An important conclusion is that the rock-concrete interface has a significant DTS when compared to those of rock and concrete [5], [13], and sometimes at the same level as that of the concrete [22]. Besides, an experimental study conducted on the tensile strength at the rock-concrete interface revealed that the DTS of bi-material specimens was lower than the indirect tensile strength (ITS) obtained from the Brazilian test [16]. In addition, the literature review shows that the failure properties and the tensile strength of rock-concrete bi-material specimens subjected to the tensile loading are controlled by various parameters, including the interface roughness, interface inclination angle, rock type, and concrete properties [1], [14], [15], [21], [23], [24].

Although some efforts have been devoted to the tensile behaviour of RC interfaces, there is still a lack of understanding of the failure mode and the fracturing mechanism of the RC interface under tension, especially on the microscale.

The main objective of this paper is to study the mechanical and failure properties of bi-material interfaces at the microscopic scale. For this purpose, direct tension experiments were conducted on prismatic rock-mortar specimens with smooth and rough interfaces. The acoustic emission (AE) and the digital image correlation (DIC) technique were used to monitor the spatiotemporal distribution of damage in the specimen from crack initiation

to final failure. The cracking mechanisms (shear, tensile, or compression) were also investigated by applying the moment tensor inversion method to explain better the relationship between micro- and macro cracking mechanisms.

2 METHODOLOGY

2.1 Materials and specimen preparation

The prismatic rock-mortar specimens with dimensions $100 \times 37 \times 30$ mm (length (L) \times width (W) \times depth (D)) were tested under the direct tension test (Fig. 1c). The mortar used in the test has a mixing weight ratio of 0.18 (water/SikaGrout 212). The rock part is Stanstead granite (Eastern Township region, Quebec, Canada), which is coarse-grained with an average grain size of 1.1 mm. The granite is mainly composed of alkali feldspar (orthoclase), plagioclase (albite), quartz, mica (biotite), and opaque minerals [25]. The basic properties of the materials are given in Table 1. Two groups of granite-mortar specimens were prepared, including group 1 with a smooth interface (F) and group 2 with a rough interface (R). The smooth interface was created by saw cutting of the granite, and the rough interface was generated by breaking granite by three-point bending (TPB). Afterward, granite was put into moulds, and mortar was cast over them. The moulds were removed after 24 hours, and the specimens were cured in a humid room for more than 28 days. After more than 28 days, the prismatic specimens' ends were polished and then glued onto the loading plates with a strong adhesive epoxy. Fig. 1a shows an example of the prepared specimens ready for the test.

Table 1. Mechanical and physical properties of the materials

Parameter	Granite	Mortar
Uniaxial compressive strength, UCS (MPa)	137.0	58.1
Modulus of elasticity, E (GPa)	50.6	29.0
Poisson's ratio, ν	0.23	0.19
P-wave velocity, V_p (km/s)	4.07	4.17
Density, ρ (kg/m ³)	2643	2265

2.2 Experimental System and Testing Methodology

Fig. 1b presents a schematic view of the three experimental observations, including load-displacement measurements, image acquisition, and Acoustic emission (AE).

2.2.1 Loading System

The direct tension tests with a displacement control mode at a rate of $1 \mu\text{m/s}$ were performed with INSTRON 4482 dual-column Universal Testing machine at the Laboratory

of Rock Mechanics of the Université de Sherbrooke. The load cell capacity is 100 KN. Two LVDT displacement transducers (Solartron Metrology, Model 925604 DCR15) measured the axial displacement along the loading direction.

2.2.2 Acoustic Emission (AE) Monitoring

The Physical Acoustics Co. (PAC) μ -SAMOS system, consisting of two 8-channel AE data acquisition systems (PCI-8), was used to collect AE data during experiments. Eight Nano-30 AE sensors with a 125–750 kHz bandwidth were employed to capture AE signals. The sensors were placed on the specimens' left, right, and back sides. The sensors were first attached to the surface of specimens using a double-sided adhesive tape (DSAT) and then glued to the specimens with hot glue, as shown in Fig. 1a and c.

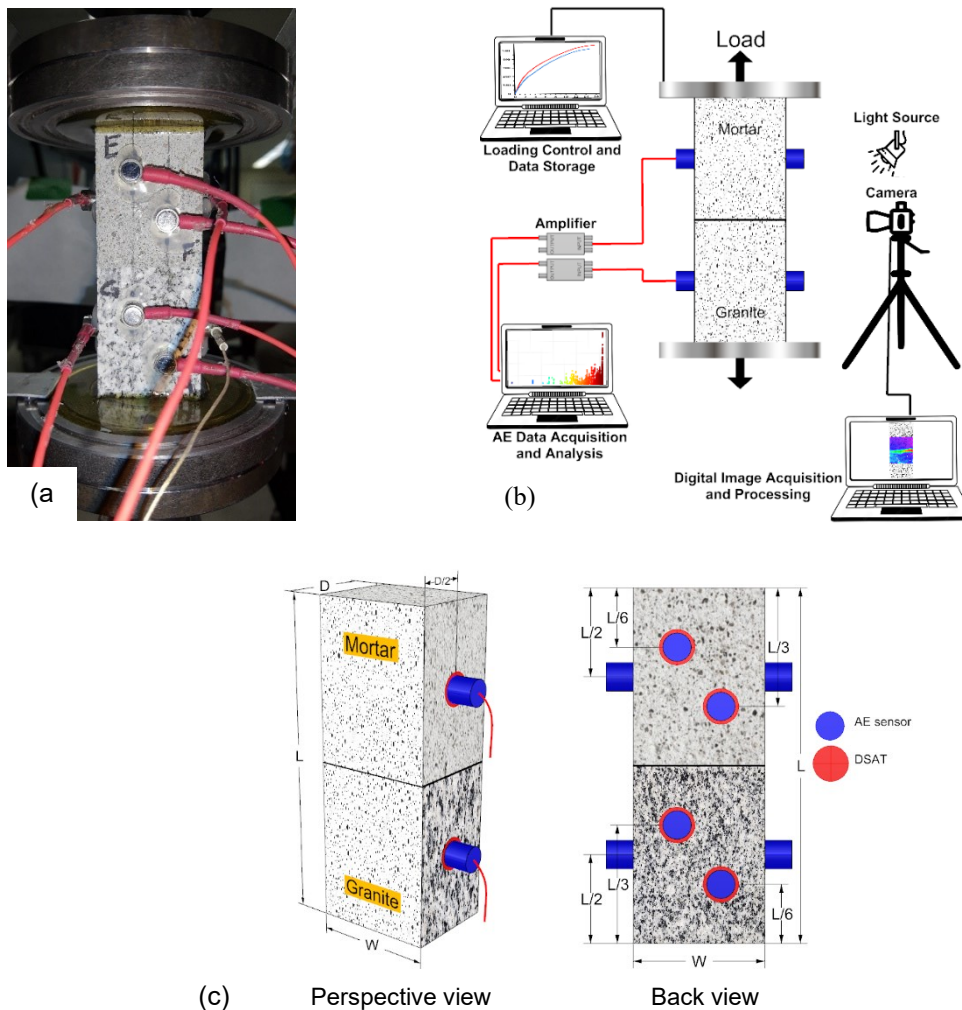


Fig. 1. (a) Example of a prismatic granite-mortar specimen glued onto the loading platens mortar (back view of the specimen), (b) schematic view of the experimental observations, including loading system, AE monitoring device, and imaging system for the 2D DIC analysis, and (c) sensor positioning on a specimen (perspective and back views). The specimen's front surface is covered by high-contrast black spackles sprayed over a white layer of paint. The specimen's dimensions are $L = 100$, $W = 37$, and $D = 30$.

The auto sensor test (AST) was also conducted to verify the efficiency of sensor-specimen coupling [26].

Full-waveform AE data were recorded using a threshold value of 35 dB at a sampling frequency of 3 MHz, with a pre-trigger of 50 μ s and a sample length of 4k. Each detected AE signal was amplified by PAC 2/3/4

preamplifiers with an amplification of 40 dB. The PDT (Peak Definition Time), HDT (Hit Definition Time), and HLT (Hit Lockout Time) parameters were set to 200, 800, and 350 μ s, respectively. The maximum duration was 10 ms.

The AE source localization was done by picking up the relative arrival time of the P-waves at each sensor using the Akaike information criterion (AIC) [27], [28]. A constant

P-wave velocity field model was applied to locate AE sources for a minimum distance error of 3 mm and optimized using the “fmincon” function in MATLAB. It should be noted that the source localization procedure requires that each event trigger a minimum of four observation points (AE sensors) to determine the four unknowns, including the event origin coordinates (x, y, z) and the event time (t). However, to increase the accuracy of the localized AE events, the source localization was also performed for a minimum of six AE sensors in order to investigate the AE source mechanism.

2.2.3 Digital Image Correlation Technique

A Basler acA2440-75um camera along with a Scheinder Xenoplan 1.9/35-0901 CM120 BK 15 compact lens was used to capture images of the specimen’s surface with a resolution of 5 (2448 × 2048) megapixel at one fps. Two LED light sources were also used to provide constant lighting over the specimen’s surface throughout the experiments (Fig. 1b). Furthermore, the specimen’s surface was covered by a black and white speckle pattern to enhance the DIC post-processing measurements (Fig. 1b and c) [29]. After capturing images, the DIC technique (using VIC-2D software (CorrelatedSolutions 2020)) was used to compute full-field displacement and strain data at the surface of the specimens.

The DIC technique uses a correlation algorithm to compare (in pixel scale) the images captured at different deformation stages and computes displacement and strain fields over a region of interest (ROI) on the specimen’s surface [29].

At the beginning of the experiments, all observation systems, including loading, imaging, and AE monitoring, were synchronized to record experimental data simultaneously.

2.2.4 Fracture Roughness Characterization

The surface roughness of the rock-mortar interface before and after the experiments was characterized. A high-accuracy 3D laser scanner (Kreon Zephyr© 25) was employed to scan the interface’s surface. 2D profiles were extracted from the acquired 3D point cloud, for which roughness parameter Z2 (the root mean square of the first deviation of the roughness profiles) was computed [31]. The Z2 value of the interface corresponds to the average of Z2 values of all 2D profiles.

3 RESULTS AND DISCUSSION

3.1 Tensile Strength and Behaviour

The load-displacement response of two specimens for each interface type (smooth and rough) is illustrated in Fig. 2. The inset shows the specimen’s corresponding nominal tensile strength (NTS), which equals the ratio of the load at the failure to the nominal surface area of the rock-mortar interface. The nominal tensile strength of the specimens with rough interfaces (with an average of 2.47 MPa) is higher than that of specimens with a smooth interface (with

an average of 2.12 MPa). This is an average difference of 16.5%. This suggests that the increase of the surface roughness increases the tensile strength of bi-material specimens. Some previous studies obtained similar findings, stating that the indirect tensile strength of bi-material Brazilian discs increased with the interface roughness [14], [15], [24]. Zhu et al. [14] and Qiu et al. [24] reasoned that with the increase of the roughness, the contact area and the interlocking (anchorage) between rock and mortar increases. This, in turn, increases the tensile strength of the bi-material specimens. The same explanation applies here.

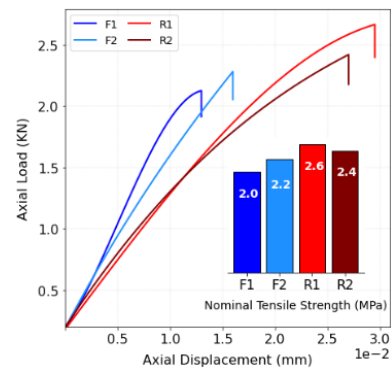


Fig. 2. Load-displacement measurements for specimens with smooth (F1 and F2) and rough (R1 and R2) interfaces. The inset bar chart indicates the corresponding nominal tensile strengths.

Fig. 3 depicts the surface morphology of the rock-mortar interface for F1 and R1 after the experiments. As seen for F1, the failure occurred both along the interface and within the mortar (as some mortar remained on the granite surface, shown by red lines). However, for R1, the failure occurred along the interface, within the mortar (as some mortar remained on the granite surface shown by red lines), and within the granite (as some granite remained on the mortar surface shown by blue lines). Therefore, it can be concluded that the tensile strength of rock-mortar specimens is governed by the interfacial adhesive strength and the cohesive strength of the mortar. In the case of rough interfaces, it appears that granite’s cohesive strength plays a role and contributes to an increase in the tensile strength of bi-material specimens. This is confirmed by the DIC and AE results given in the next sections. It should be mentioned that the damage in granite in R1 suggests that with the increase of the roughness, the interfacial adhesive strength (interlocking between rock and mortar) may even exceed the cohesive strength of granite. A similar conclusion was achieved by Luo et al. [21].

As mentioned, the tensile strength reported in Fig. 2 is the nominal tensile strength. An attempt was made to compute the true tensile strength (TTS) of specimens, which is defined as the ratio of the load at the failure to the actual surface area of the generated macroscopic fracture. For this purpose, the surface of macroscopic fractures was scanned, a 3D point cloud was obtained, and a

triangulated 3D mesh was produced. The true surface area was then computed from the generated mesh. The nominal and true tensile strengths and their differences are given in Table 2. For both specimen groups, F and R, the TTS is smaller than the NTS. This might be an essential point when reporting the tensile strength of materials. In addition, the difference between the average true tensile strength of F and R specimens is now 13.5%. It means, by considering the TTS instead of the NTS, the effect of roughness on tensile strength is relatively less important.

Moreover, the load-displacement curves in Fig. 2 indicate that the failure in group R specimens was more ductile than that in group F. That is, increasing the roughness of the rock-mortar interface resulted in less brittle failure. This could be due to the occurrence of more microcracks during a longer period of loading duration in R specimens, which is more evident by looking at the AE and DIC results discussed in the next sections.

From the energy aspect, the total external work (W) by the applied load is decomposed into internal damage and frictional loss [32]. The external work (the area under the load-displacement curves) was calculated for all specimens, which are 16.5 mJ and 20.9 mJ for F1 and F2, and 48.4 mJ and 40.6 mJ for R1 and R2, respectively. Here, by neglecting the frictional loss component of the external work, we can suppose that 100 % of the work was converted to internal damage to specimens. Therefore, by considering the higher values of the external work for the group R specimens, it can be concluded that there was more micro-damage to R1 and R2 during the loading period. This explains the ductile behaviour of R specimens under tensile loading.

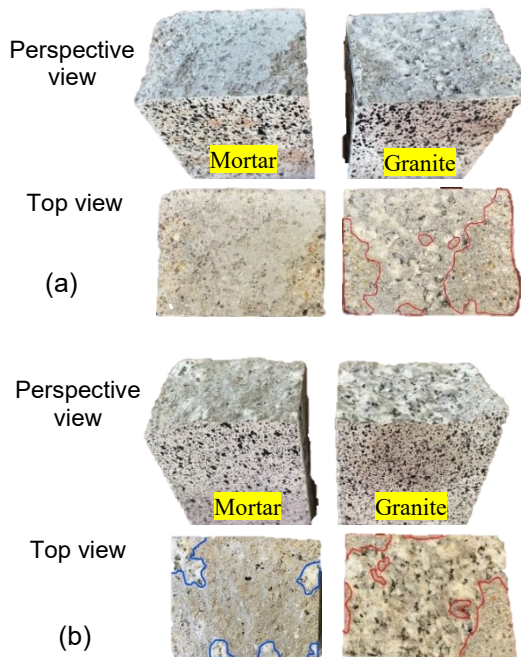


Fig. 3. Surface morphology of the granite-mortar interface after failure for (a) F1 and (b) R1. Red lines represent the remaining mortar on the granite surface, and blue lines show the remaining granite on the mortar surface.

Table 2. Specimens' nominal and true tensile strength

Specimen	NTS (MPa)	TTS (MPa)	Difference (%)
F1	2.00	1.90	-5.0
F2	2.24	2.20	-1.8
R1	2.58	2.39	-7.4
R2	2.36	2.27	-3.8

NTS: Nominal tensile strength, TTS: True tensile strength

3.2 Temporal Evolution of Fracturing Processes

Erreur ! Source du renvoi introuvable. shows the load-displacement data, the cumulative rate of AE hits, and the amplitudes of AE hits over the loading process for F1 and R1. In general, AE hits reflect damage to the inspected material. In addition, hits with higher amplitudes indicate more severe damage. Fig. 4a shows no AE activity before reaching 51% of peak load (F_p), where the first AE hits were detected. These small-amplitude hits may be because of internal damage to the specimen or be noises. However, there is a noticeable inflection in the AE cumulative at F_p with increasing the load. A considerable number of relatively high-amplitude hits appeared, followed by a reduction in AE hit numbers. A closer inspection of the load-displacement data (see inset in Fig. 4a) indicated that these clusters of AE hits correspond to a small load drop in the load-displacement curve. This may be due to a local adhesion loss along the rock-mortar interface, as, in particular, there is a reduction in both the AE hit numbers and AE amplitudes for a while after this load drop. There is a second inflection in the cumulative hits curve at 85% failure load, after which the rate of AE hits increases constantly. This continuous increase in AE hits indicates the start of the microcracks within the specimen after the second inflection point. The accumulation of micro-damage leads to the ultimate failure that appears as a sharp growth in the cumulative hits at the failure load. As observed, the sharp growth consists of high-amplitude AE hits.

For R1, the AE hits started to occur at 41% F_p (Fig. 4b). However, the consistent increasing trend in the cumulative hits curve suggests that the micro-damage began and accumulated gradually when the interface was rough. In addition, the higher number of AE hits in Fig. 4b shows that R1 underwent more internal damage (more micro-cracks) than F1 throughout the loading process. This difference can be explained as follows. As shown in Fig. 3, for F1, only the damage in the interface plus within the mortar contributed to the macroscopic damage. In contrast, for R1, the damage in granite contributed to the final macroscopic failure. Hence, this is the damage in the granite that may have produced a higher number of AE hits in R1 than in F1. This is also confirmed by evaluating the process zone obtained by AE and DIC analyses, which are discussed below.

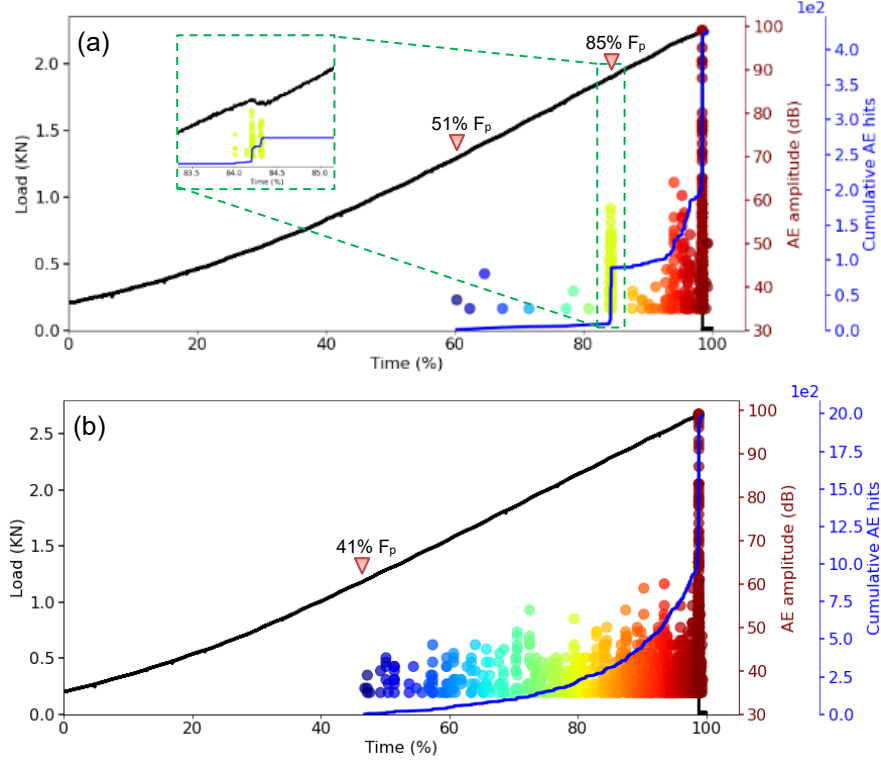


Fig. 4. Load-displacement (black line), AE amplitude (scatter data), and cumulative AE hits (blue line) for (a) F1 and (b) R1. F_p denotes the failure load. For the scatter data, the colour is encoded with the test time.

3.3 Spatial Evolution of Fracturing Processes

The spatial distribution and the number of located AE events for the specimens F1 and R1 are illustrated in Fig. 5a and 5b, respectively. In Fig. 5, the blue lines represent the observed ultimate macroscopic fracture. Here, AE signals that were detected by four sensors were counted as an AE event. 11 and 46 AE events were detected for F1 and R1, respectively, indicating that the specimen with a rough interface experienced a higher number of microcracks. In both cases, the event locations coincide well with the macroscopic fracture trace (blue lines in Fig. 5), and most AE events occurred within the mortar part as the weaker material.

AE source mechanisms were determined using the moment tensor inversion (MTI) to further investigate the properties of AE events. The MTI was performed on events with six or more P-wave arrival detections according to the 2D implementation of the SIGMA (Simplified Green's functions for Moment tensor Analysis) procedure [33]. Moment tensors were decomposed into double-couple (DC), isotropic (ISO), and compensated linear vector dipole (CLDV) components for each event, according to Vavryčuk [34]. Then, AE events were considered as shear ($|ISO| < 15\%$), compaction ($ISO \leq -15\%$ and $CLVD \leq 15\%$), and tensile ($ISO \geq 15\%$ and $CLVD \geq -15\%$) events [35].

The focal mechanism of the AE events is shown in Fig. 5c and 5d for F1 and R1. Here, the AE events detected by four sensors are also illustrated with pale gray circles. The

colour bar in Fig. 5c and 5d reflect the average focal amplitude (A_0) of the AEs calculated considering geometrical spreading for a reference distance of 10mm as in Zang et al. (1998):

$$A_0 = \sqrt{\frac{1}{n} \sum_{i=1}^n \left(A_i \frac{r_i}{10} \right)^2} \quad [1]$$

Where n is the number of sensors receiving the same AE signal, A_i is the first motion signal amplitude received by the i^{th} sensor, and r_i (in mm) is the signal source distance to the i^{th} sensor.

There are only 4 AE events detected by at least six sensors for F1, while it was 14 for R1. All 4 AE events for F1 have tensile sources. Although there are a very low number of AE events for F1, it can be inferred that the macroscopic cracking mechanism for the specimen with the smooth interface is primarily tensile, as expected. Therefore, it can be concluded that both macroscopic and microscopic fracturing mechanisms are tensile in the case of the smooth interface.

Among 14 AE events detected for R1, there are 8 tensile, 3 shear, and 3 compressive events (microcracks). Again, most AE events are of tensile type. However, the existence of shear sources can be attributed to the internal damage in granite, as some part of the granite was broken

and remained on the mortar surface (blue lines in Fig. 3b). More importantly, the existence of shear microcracks can explain why the tensile strength of R1, with a rough interface, is higher than that of F1, with a smooth interface. In fact, in the case of F1, only the micro-tensile cracking mechanism contributes to the macroscopic fracture. In contrast, for R1, both micro-tensile and micro-shear

cracking mechanism play their roles in macroscopic fracturing. Therefore, as micro-shear cracks have higher strength than micro-tensile ones [10], [11], the macroscopic tensile strength of R1 exceeded that of F1.

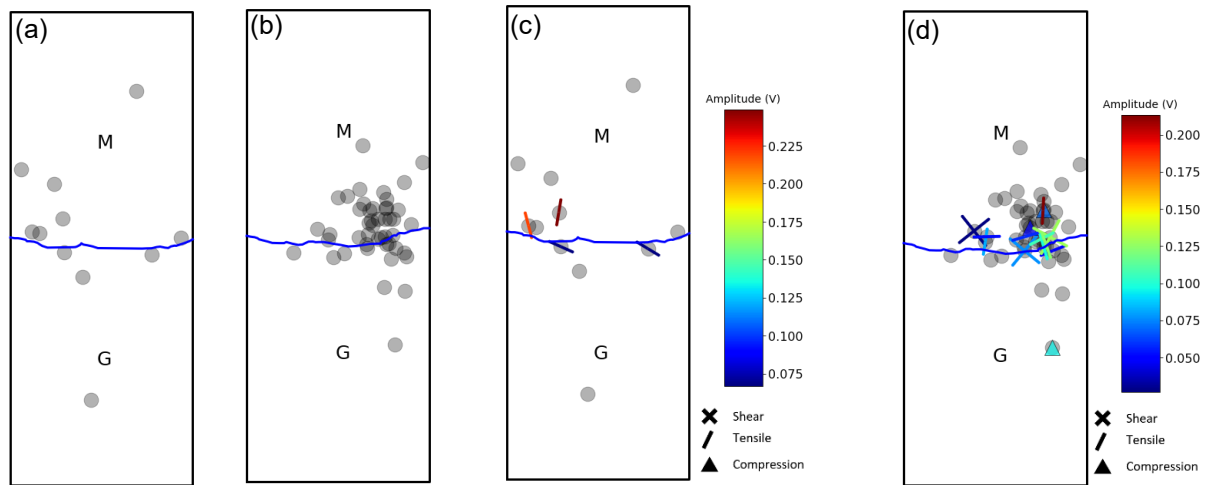


Fig. 5. Spatial distribution of the AE events within the specimen (a) F1 and (b) R1, and AE source mechanism for (c) F1, (d) R1. The colour of AE events represents their magnitude. G and M denote the granite and the mortar parts.

Fig. 6 shows a schematic representation of microcracking mechanisms for rock-mortar specimens with smooth (F1) and rough (R1) interfaces. Due to the interlocking (anchorage) between rock and mortar (Fig. 6b), both tensile and shear microcracks can occur during the damage process of R1. However, for the smooth

interface specimen (F1), the applied tensile load can predominantly result in tensile microcracks (Fig. 6a). This explains why there are some shear-type sources in AE events detected for R1 while all AE events for F1 are of tensile-type.

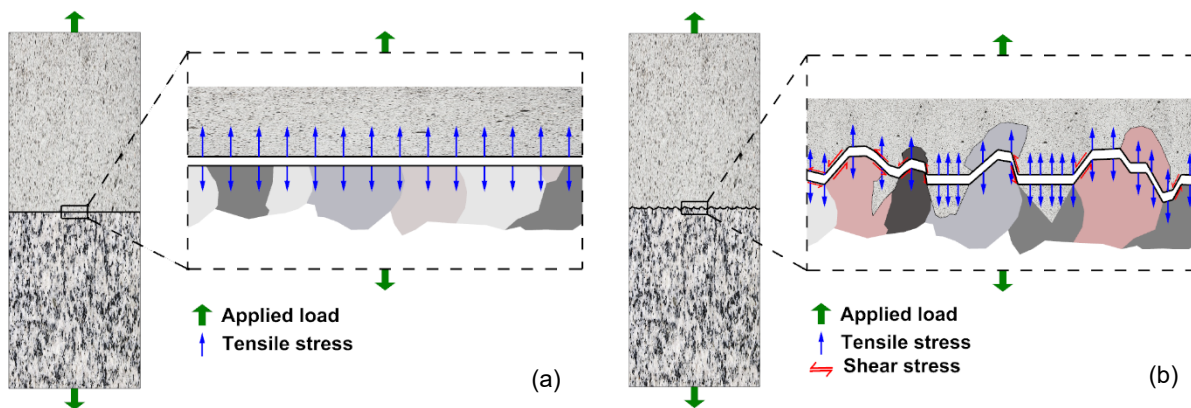


Fig. 6. A schematic representation of the applied load and the induced microcracking mechanisms for specimen with (a) smooth, F1 and (b) rough, R1 interfaces.

The 2D DIC analysis, implemented using the software VIC-2D (CorrelatedSolutions, 2020), was applied to determine the strain fields over the specimen's surface.

The area of interest (AOI), over which the measurements were performed, covers the middle part of bi-material specimens, where the ultimate failure occurred. A subset size of 29×29 pixels was chosen to ensure a unique

speckle pattern within each subset. Also, a step size of 7 pixels was picked between subsets to get independent and non-repetitive data points over the surface of the specimen (CorrelatedSolutions, 2020; Sutton et al., 2009).

Fig. 7a and b display the process zone obtained from DIC analysis for F1 and R1, respectively. The DIC process zone shows the nominal tensile strain immediately before failure in the vertical (loading) direction (ϵ_{yy}). The colour bars in Fig. 7 represent the extensional strain distribution

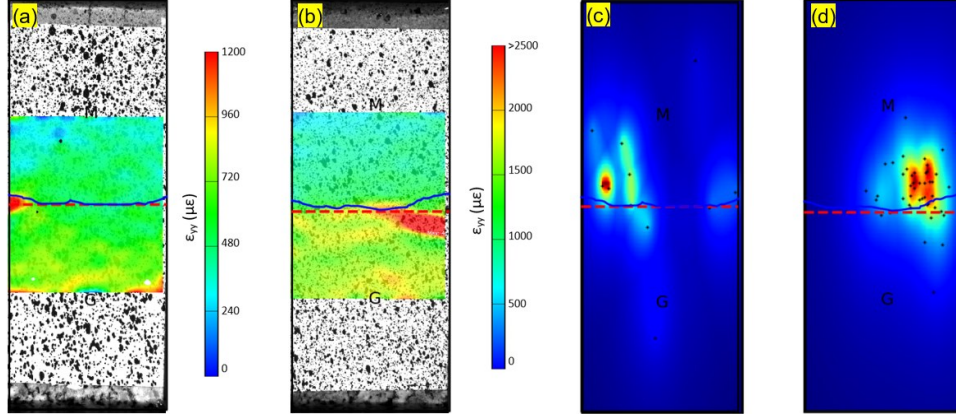


Fig. 7. Vertical (ϵ_{yy}) strain field immediately prior to failure for (a) F1 and (b) R1, and scatter plot of AE distributions coloured by density for (c) F1 and (d) R1. Darker shades of red indicate higher concentrations of AE events. The red dash lines represent the location of the interface, while the solid blue lines represent the trace of the macroscopic fracture.

Generally, the AE-based and DIC-based process zones are in good agreement for both specimens. The DIC measurements indicated that the maximum value of the nominal tensile strain right before failure was 1100 $\mu\epsilon$ and 3900 $\mu\epsilon$ for F1 and R1, respectively. This is consistent with the maximum value of axial displacements for the group F and R specimens shown in Fig. 2. In addition, as Fig. 7 indicates, both the AE and DIC plots clearly show that the specimen with a rough interface, i.e., R1, had a larger process zone before the final failure. This suggests that R1 underwent more micro fracturing before reaching the final failure, hence, justifying the more ductile behaviour of the group R specimens in Fig. 2.

More importantly, the DIC process zone for F1 and R1 shows that maximum values of the tensile strain accumulation occurred almost along the interfaces (shown in red dash-lines in Fig. 7). However, the AE process zone shows that AE events are mostly concentrated in the mortar (upper) parts of specimens, hence better approximates the location of the macroscopic fractures (shown in solid blue lines in Fig. 7). This difference could be, to some extent, because the measurements in DIC are limited to the information on the exterior surfaces of specimens, while AE events reflect deformation in the whole volume of the specimen.

in the ROI. In addition, Fig. 7c and d show the scatter plot of the detected AEs coloured by density for F1 and R1. These density plots reveal the extent of the AE-based process zone. Darker shades of red indicate a higher concentration of AE events, and darker shades of blue indicate lower AE activities. The red dash lines represent the location of the rock-mortar interface, and the solid blue lines indicate the trace of the macroscopic fractures.

3.4 Roughness Characterization of the Generated Macroscopic Fractures

To compare the roughness of the interface before tests with that of the macro fractures, the surface of the granite segments (before mortar casting and after tests) was scanned using a laser scanner. The interface's 3D morphology before testing for F1 and R1 is shown in Fig. 8a, and their morphology after failure is shown in Fig. 8b. Qualitatively, it is seen that the surface of R1 is still rougher than F1, which was expected because the majority of the failure along the interface was adhesive loss (interface detachment) for both specimens.

The roughness of the scanned surfaces was then quantified using the root mean square of the first deviation of the roughness profiles (Z2) as follows [31]:

$$Z2 = \left[\frac{1}{n(\Delta y)^2} \sum_{i=1}^n (z_{i+1} - z_i)^2 \right]^{1/2} \quad [2]$$

Where n is the number of sampling points along the 2D roughness profiles, $\Delta y = y_{i+1} - y_i$ is the constant interval between adjacent points, and $z_{i+1} - z_i$ is the height difference between two adjacent points.

The Z2 values in the x and y directions for R1 and F1, before and after tests, are displayed in Fig. 8c. The Z2 value of F1 increased from 0.1 to 0.2 in both the x and y directions, while these values did not change a lot for R1.

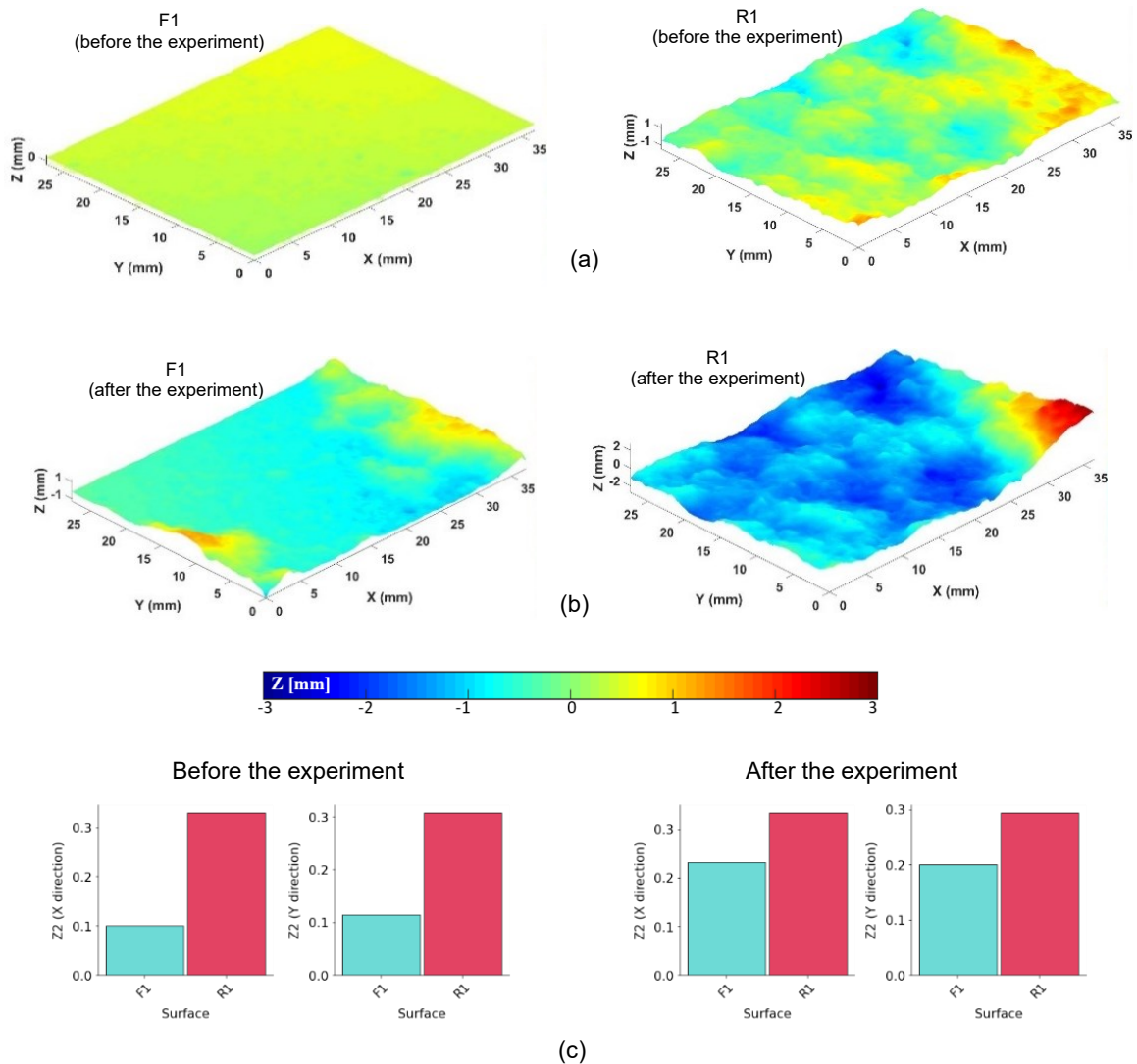


Fig. 8. The 3D surface of (a) F1 and R1 (before the experiment), (b) F1 and R1 (after the experiment), and (c) Zz value for F1 and R1 in x and y directions (before and after the experiment). The same legend scale is applied to all 3D morphology plots.

4 CONCLUSIONS

The AE and DIC measurements were simultaneously employed to study the tensile strength and the fracturing properties of the rock-mortar bi-materials under direct tension. The main contributions of this study can be summarized as follows:

With the increase in interface's roughness, the tensile strength of rock-mortar specimens increases. In fact, with increasing the roughness, the anchorage between rock and mortar increases resulting in a higher nominal tensile strength. However, when the true tensile strength is considered, the increase in tensile strength with roughness will be less significant.

Increasing the interface's roughness also resulted in a more ductile deformation in specimens, as reflected in load-displacement curves. As the cumulative AE hits showed, the specimens with a rough interface underwent more progressive micro-damage during the loading process. This was also seen in both the AE and DIC results.

The temporal evolution of AE hits showed that AEs could be used as a precursor in studying the fracturing process of bi-material specimens. However, the AE activity is more prominent for specimens with rough interfaces.

The AE process zone was relatively larger than the DIC process zone for smooth and rough interfaces. This is mainly because the DIC can only monitor the surface deformations, while AEs are micro damages in the whole

volume of the specimen. Thus, the AE process zone may more accurately determine the fracturing process in specimens.

The DIC process zone indicated that the tensile strains were mostly accumulated along the rock-mortar interfaces; however, the final fracture path did not pass these strain concentration zones. On the other hand, the AE process zone showed that AE events mainly concentrated where the final macroscopic fractures occurred. This again suggests that the AE-based process zone may be more reliable than the DIC-based.

REFERENCES

- Andjelkovic, V., Pavlovic, N., Lazarevic, Z., & Nedovic, V. (2015). Modelling of shear characteristics at the concrete-rock mass interface. *International Journal of Rock Mechanics and Mining Sciences*, 76, 222–236. <https://doi.org/10.1016/j.ijrmms.2015.03.024>
- Barrett, S. V. L., & McCreath, D. R. (1995). Shortcrete support design in blocky ground: Towards a deterministic approach. *Tunnelling and Underground Space Technology Incorporating Trenchless*, 10(1), 79–89. [https://doi.org/10.1016/0886-7798\(94\)00067-U](https://doi.org/10.1016/0886-7798(94)00067-U)
- Biolzi, L., Cattaneo, S., & Rosati, G. (2001). Flexural/tensile strength ratio in rock-like materials. *Rock Mechanics and Rock Engineering*, 34(3), 217–233. <https://doi.org/10.1007/s006030170010>
- Chang, X., Lu, J., Wang, S., & Wang, S. (2018). Mechanical performances of rock-concrete bi-material disks under diametrical compression. *International Journal of Rock Mechanics and Mining Sciences*, 104(November 2017), 71–77. <https://doi.org/10.1016/j.ijrmms.2018.02.008>
- CorrelatedSolutions. (2020). Vic-2D 2020 Reference Manual. Columbia, SC, USA. Retrieved June 2, 2021, from www.CorrelatedSolutions.com
- Cuccovillo, T., & Coop, M. R. (1999). On the mechanics of structured sands. *Géotechnique*, 49(6), 741–760.
- Electric Power Research Institute (EPRI). (1992). *Uplift pressures, shear strengths and tensile strengths for stability analysis of concrete gravity dams*.
- Flansbjerg, M., & Magnusson, J. (2014). *Mechanical properties of rock-concrete interface*. Retrieved from www.skb.se.
- Griffith, A. (1924). The theory of rupture. *First Int. Cong. Appl. Mech*, 55–63.
- Grosse, C. U., & Ohtsu, M. (2008). *Acoustic Emission Testing. Basic for Research-Applications in Civil Engineering* (Vol. 53). Springer. Retrieved from <http://www.elsevier.com/locate/scp>
- Gutiérrez-Ch, J. G., Senent, S., Melentijevic, S., & Jimenez, R. (2018). Distinct element method simulations of rock-concrete interfaces under different boundary conditions. *Engineering Geology*, 240(November 2017), 123–139. <https://doi.org/10.1016/j.enggeo.2018.04.017>
- Iqbal, M. J., & Mohanty, B. (2006). Experimental calibration of stress intensity factors of the ISRM suggested cracked chevron-notched Brazilian disc specimen used for determination of mode-I fracture toughness. *International Journal of Rock Mechanics and Mining Sciences*, 43(8), 1270–1276. <https://doi.org/10.1016/j.ijrmms.2006.04.014>
- Jawalkar, C. K. M. (1996). Interface cracks: fracture mechanics studies leading towards safety assessment of dams. University of Colorado at Boulder.
- Kodikara, J. K., & Johnston, I. W. (1994). Shear behaviour of irregular triangular rock-concrete joints. *International Journal of Rock Mechanics and Mining Sciences And*, 31(4), 313–322. [https://doi.org/10.1016/0148-9062\(94\)90900-8](https://doi.org/10.1016/0148-9062(94)90900-8)
- Kurz, J. H., Grosse, C. U., & Reinhardt, H. W. (2005). Strategies for reliable automatic onset time picking of acoustic emissions and of ultrasound signals in concrete. *Ultrasonics*, 43(7), 538–546. <https://doi.org/10.1016/j.ultras.2004.12.005>
- Li, B. Q., da Silva, B. G., & Einstein, H. (2019). Laboratory hydraulic fracturing of granite: Acoustic emission observations and interpretation. *Engineering Fracture Mechanics*, 209, 200–220.
- Li, L. R., Deng, J. H., Zheng, L., & Liu, J. F. (2017). Dominant Frequency Characteristics of Acoustic Emissions in White Marble During Direct Tensile Tests. *Rock Mechanics and Rock Engineering*, 50(5), 1337–1346. <https://doi.org/10.1007/s00603-016-1162-2>
- Luo, L., Li, X., Tao, M., & Dong, L. (2017). Mechanical behavior of rock-shotcrete interface under static and dynamic tensile loads. *Tunnelling and Underground Space Technology*, 65, 215–224. <https://doi.org/10.1016/j.tust.2017.03.005>
- Moradian, Z. A., Ballivy, G., Rivard, P., Gravel, C., & Rousseau, B. (2010). Evaluating damage during shear tests of rock joints using acoustic emissions. *International Journal of Rock Mechanics and Mining Sciences*, 47(4), 590–598. <https://doi.org/10.1016/j.ijrmms.2010.01.004>
- Mouzannar, H., Bost, M., Leroux, M., & Virely, D. (2017). Experimental Study of the Shear Strength of Bonded Concrete–Rock Interfaces: Surface Morphology and Scale Effect. *Rock Mechanics and Rock Engineering*, 50(10), 2601–2625. <https://doi.org/10.1007/s00603-017-1259-2>
- Ohno, K., & Ohtsu, M. (2010). Crack classification in concrete based on acoustic emission. *Construction and Building Materials*, 24(12), 2339–2346. <https://doi.org/10.1016/j.conbuildmat.2010.05.004>
- Perras, M. A., & Diederichs, M. S. (2014). A Review of the Tensile Strength of Rock: Concepts and Testing. *Geotechnical and Geological Engineering*, 32(2), 525–546. <https://doi.org/10.1007/s10706-014-9732-0>
- Qiu, H., Zhu, Z., Wang, M., Wang, F., Luo, C., & Wan, D. (2020). Study of the failure properties and tensile strength of rock-mortar interface transition zone using bi-material Brazilian discs. *Construction and Building Materials*, 236, 117551. <https://doi.org/10.1016/j.conbuildmat.2019.117551>
- Saiang, D., Malmgren, L., & Nordlund, E. (2005). Laboratory tests on shotcrete-rock joints in direct

- shear, tension and compression. *Rock Mechanics and Rock Engineering*, 38(4), 275–297. <https://doi.org/10.1007/s00603-005-0055-6>
- Selçuk, L., & Aşma, D. (2019). Experimental investigation of the Rock–Concrete bi materials influence of inclined interface on strength and failure behavior. *International Journal of Rock Mechanics and Mining Sciences*, 123(June), 123–149. <https://doi.org/10.1016/j.ijrmms.2019.104119>
- Son, M. (2013a). Adhesion strength at the shotcrete–rock contact in rock tunneling. *Rock Mechanics and Rock Engineering*, 46(5), 1237–1246. <https://doi.org/10.1007/s00603-013-0380-0>
- Son, M. (2013b). Adhesion strength at the shotcrete–rock contact in rock tunneling. *Rock Mechanics and Rock Engineering*, 46(5), 1237–1246. <https://doi.org/10.1007/s00603-013-0380-0>
- Sutton, M. A., Orteu, J. J., & Schreier, H. (2009). *Image correlation for shape, motion and deformation measurements: basic concepts, theory and applications*. Springer Science & Business Media.
- Tian, H. M., Chen, W. Z., Yang, D. S., & Yang, J. P. (2014). Experimental and Numerical Analysis of the Shear Behaviour of Cemented Concrete–Rock Joints. *Rock Mechanics and Rock Engineering*, 48(1), 213–222. <https://doi.org/10.1007/s00603-014-0560-6>
- Vavryčuk, V. (2015). Moment tensor decompositions revisited. *Journal of Seismology*, 19(1), 231–252. <https://doi.org/10.1007/s10950-014-9463-y>
- Yang, Z. Y., Lo, S. C., & Di, C. C. (2001). Reassessing the joint roughness coefficient (JRC) estimation using Z2. *Rock Mechanics and Rock Engineering*, 34(3), 243–251. <https://doi.org/10.1007/s006030170012>
- You, M. (2015). Strength criterion for rocks under compressive-tensile stresses and its application. *Journal of Rock Mechanics and Geotechnical Engineering*, 7(4), 434–439. <https://doi.org/10.1016/j.jrmge.2015.05.002>
- Zang, A., Wagner, F. C., Stanchits, S., Dresen, G., Andresen, R., & Haidekker, M. A. (1998). Source analysis of acoustic emissions in Aue granite cores under symmetric and asymmetric compressive loads. *Geophysical Journal International*, 135(3), 1113–1130. <https://doi.org/10.1046/j.1365-246X.1998.00706.x>
- Zhou, Z., Lu, J., & Cai, X. (2020). Static and dynamic tensile behavior of rock-concrete bi-material disc with different interface inclinations. *Construction and Building Materials*, 256, 119424. <https://doi.org/10.1016/j.conbuildmat.2020.119424>
- Zhu, J., Bao, W., Peng, Q., & Deng, X. (2020). Influence of substrate properties and interfacial roughness on static and dynamic tensile behaviour of rock-shotcrete interface from macro and micro views. *International Journal of Rock Mechanics and Mining Sciences*, 132, 104350. <https://doi.org/10.1016/j.ijrmms.2020.104350>